Pergamon

Int. J. Multiphase Flow Vol. 24, No. 2, pp. 319–334, 1998

Printed in Great Britain

PII: S0301-9322(97)00057-8

0301-9322/98 $19.00 + 0.00

CALCULATION OF DRYOUT AND POST-DRYOUT HEAT TRANSFER FOR TUBE GEOMETRY

NORBERT HOYER

Nuclear Engineering, Scandpower A/S, PO Box 3, N-2007 Kjeller, Norway

(Received 26 January 1996; in revised form 4 June 1997)

Abstract—A method for calculating dryout power and post-dryout heat transfer in tube geometry is described and validation results are presented. A two-phase, three-field annular flow model is utilized, which bases dryout on the criterion of a disappearing liquid film at the wall. Entrainment and deposition are key phenomena and have to be adequately modelled, including the effect of wall heat flux. The calculational method is tested in the framework of the MONA code and validated against the KTH dryout experiments. The model generally provides good results for dryout position and power, and successfully takes account of variations in tube diameter, pressure, and mass and heat flux. The model predicts the effect of a varying axial heat flux distribution especially well, as mechanisms like heat flux induced entrainment and deposition inhibition through film evaporation are accounted for. Also post-dryout heat transfer predictions agree well with little systematic deviation and correct shapes of the temperature profiles. © 1998 Elsevier Science Ltd. All rights reserved

Key Words: annular flow, dryout model, post-dryout heat transfer

1. INTRODUCTION

In a nuclear reactor, the power generated is often limited by the value at which the rod surface is no longer wetted by the boiling liquid. At that point the heat transfer coefficient drops dramatically and leads to the onset of a surface temperature excursion. The respective heat flux is denoted critical heat flux (CHF) and is an important parameter to predict in safety analysis.

There are basically two classes of CHF situations: departure from nucleate boiling (DNB) and dryout (DO). The latter is also sometimes called burnout or departure from forced convective boiling in vapor–continuous flow. DNB is often related to subcooled boiling and can be associated with phenomena like microlayer evaporation under a bubble, bubble crowding or vapor blanketing at the wall. It has been difficult for a long time to develop DNB models that actually describe the physical processes involved and which can be used for predicting the CHF-situation with good accuracy, and consequently, empirical correlations have been applied. In the last two decades mechanistic models have been developed and reviews of those have been published by, among others, Weisman (1992); Celata *et al.* (1994); Katto (1994); Bricard and Souyri (1995). In contrast to the empirical correlations which are valid over relatively narrow ranges, the latter models should have a wider range of applicability.

For DO, on the other hand, the mechanism is much better established and several analytical approaches to predict CHF have been developed during the last 20 years. While the DNB usually occurs at bubbly or churn flow and low qualities, DO is connected to annular flow and higher qualities. The essential features of this flow regime are a liquid film flowing on the channel wall and a vapor core containing entrained droplets. These droplets are continually torn off the film, mainly due to large disturbance waves on the liquid film, and partly redeposited onto the film again.

A common starting point to existing analytical models is a three-flow-field model including the liquid film at the wall, the steam core and a separate droplet field. In case of DO the thickness of the liquid film, which results from the balance between the evaporation, entrainment and deposition rates, approaches zero. This assumption has been confirmed experimentally but may not always be valid (Milashenko *et al.* 1989). One of the first three-field annular flow models,

which gave reasonable results for flow in round tubes has been published by Whalley *et al.* (1974).

For horizontal flow, especially at low velocities, the governing phenomena may be different. As it is necessary to limit the scope of the present discussion, only static DO in vertical annular flow is considered here.

At the DO location, the liquid film disappears and no liquid is in contact with the wall and consequently the heat transfer coefficient drops dramatically. Downstream, dispersed-flow film boiling takes place and in many situations the wall temperature is an important parameter, for example for structural integrity. The dispersed-flow film boiling regime is characterized by liquid droplets in a continuous vapor phase. The major mode of heat transfer in this regime is convection to the vapor. The complexity in prediction of the heat transfer comes from the thermal nonequilibrium between the two phases, which is controlled by interfacial heat, mass and momentum transfers.

The two-phase, three-field annular flow model presented here is tested in the framework of the MONA code (Hoyer 1995) and validated against the KTH dryout experiments (Becker *et al.* 1983, 1992).

2. MODEL DESCRIPTION

For the three-flow-field model the mass balance can be written as:

Gas phase:

$$\frac{\partial}{\partial t}(\alpha\rho_{\mathrm{g}}) = -\frac{1}{A}\frac{\partial}{\partial z}\left(A\alpha\rho_{\mathrm{g}}U_{\mathrm{g}}\right) + \Psi_{\mathrm{g,l}} + \Psi_{\mathrm{g,d}} + W_{S\mathrm{g}} \qquad [1]$$

Liquid phase at the wall:

$$\frac{\partial}{\partial t}(\beta\rho_{\mathrm{l}}) = -\frac{1}{A}\frac{\partial}{\partial z}\left(A\beta\rho_{\mathrm{l}}U_{\mathrm{l}}\right) - \Psi_{\mathrm{g,l}} - \Psi_{\mathrm{e}} + \Psi_{\mathrm{d}} + W_{s\mathrm{l}} \qquad [2]$$

Liquid droplets:

$$\frac{\partial}{\partial t}(\gamma\rho_{\mathrm{l}}) = -\frac{1}{A}\frac{\partial}{\partial z}\left(A\gamma\rho_{\mathrm{l}}U_{\mathrm{d}}\right) - \Psi_{\mathrm{g,d}} + \Psi_{\mathrm{e}} - \Psi_{\mathrm{d}} + W_{\mathrm{Sd}} \qquad [3]$$

In the above equations, α, β and γ are the gas, liquid film, and liquid droplet volume fractions, ρ the density, U the velocity and A the pipe cross-section. Subscripts g, l and d indicate gas, liquid and droplets, respectively. Ψ_{g} is the mass transfer rate between the phases, Ψ_{e} and Ψ_{d} are the entrainment and deposition rates and $W_{\mathrm{S}f}$ (f = g,l,d) is a possible mass source of phase f. The mass transfer terms $\Psi_{\mathrm{g,l}}$ and $\Psi_{\mathrm{g,d}}$ are calculated by the respective heat transfer coefficients and interfacial areas of the liquid film and droplets. For the actual conditions almost all evaporation upstream the dryout location occurs at the liquid film surface.

2.1. *Entrainment and deposition rates*

A key feature in annular flow is the prediction of droplet deposition and entrainment. Correct modeling of these is a basic requirement for the calculation of dryout through a phenomenological approach based on the disappearance of the liquid film. A set of entrainment and deposition correlations have been suggested by Govan (1990). The deposition rate is correlated by:

$$\text{If } \frac{\mathrm{C}}{\rho_{\mathrm{g}}} \leq 0.3$$

$$\Psi\mathrm{d} = \frac{4}{D}0.18\sqrt{\frac{\sigma}{\rho_{\mathrm{g}}D}\mathrm{C}}$$

$$\text{If } \frac{\mathrm{C}}{\rho_\mathrm{g}} > 0.3$$

$$\Psi\mathrm{d} = \frac{4}{D}0.083\left(\frac{\mathrm{C}}{\rho_\mathrm{g}}\right)^{-0.65}\sqrt{\frac{\sigma}{\rho_\mathrm{g} D}C}$$

with

$$\mathrm{C} = \frac{G_\mathrm{d}}{\dfrac{G_\mathrm{g}}{\rho_\mathrm{g}} + \dfrac{G_\mathrm{d}}{\rho_\mathrm{l}}} = \frac{\gamma\rho_\mathrm{l}}{(\alpha+\gamma)} \qquad [4]$$

In the above equations, D is the tube diameter, σ the surface tension and G_d and G_g are the droplet and vapor mass fluxes, respectively. The deposition velocity is reduced with increasing homogeneous droplet concentration in the steam core, C. Thus the effects of pressure, surface tension and droplet concentration are included.

Having selected a deposition correlation, the rate of entrainment can be obtained with the assumption of fully developed flow and equilibrium, $\Psi_\mathrm{e} = \Psi_\mathrm{d}$. The entrainment correlation recommended by Govan and Hewitt (1990) is:

$$\Psi_{\mathrm{e},h} = \frac{4}{D}5.75\times10^{-5}\left[(\beta\rho_\mathrm{l}U_\mathrm{l} - G_{\mathrm{l}c})^2\frac{D\rho_\mathrm{l}}{\sigma\rho_\mathrm{g}^2}\right]^{0.316}\alpha\rho_\mathrm{g}U_\mathrm{g}$$

with

$$G_\mathrm{lc} = \frac{\mu_\mathrm{l}}{D}\exp\left(5.8504 + 0.4249\frac{\mu_\mathrm{g}}{\mu_\mathrm{l}}\sqrt{\frac{\rho_\mathrm{l}}{\rho_\mathrm{g}}}\right) \qquad [5]$$

where μ_g and μ_l are the vapor and liquid dynamic viscosities and G_lc is the critical film mass flux below which no entrainment occurs.

Before adopting [5] we used a modified correlation from Dallman *et al.* (1979), where the entrainment rate exhibits about the same dependency on steam density and velocity as [5]. A quadratic dependency on vapor velocity, as found in the original version, resulted in an erroneous variation of dryout location with mass flux.

The above correlations from Govan were obtained from an extensive database for fully developed annular flow. They describe hydrodynamic deposition and entrainment. However, entrainment may also be generated by the boiling process due to the release of bubbles from the liquid film. In addition, the deposition suppression effect from vaporization at the film surface may be important. Milashenko *et al.* (1989) give a dimensional correlation for the net entrainment rate due to the heat flux q (in $\mathrm{W/m^2}$).

$$\Psi_{\mathrm{e},q} = \frac{1.75}{\pi D}\beta\rho_\mathrm{l}U_\mathrm{l}\left(q\times10^{-6}\frac{\rho_\mathrm{g}}{\rho_\mathrm{l}}\right)^{1.3} \qquad [6]$$

The tube diameter used was 13.1 mm and the range of pressures was 5–10 MPa. Mass and heat fluxes ranged from 1000 to 3000 $\mathrm{kg/sm^2}$ and from 150 to 4000 $\mathrm{kW/m^2}$, respectively. The heat flux induced entrainment is negligible for the low pressure cases, but it has a considerable effect for the high pressure runs. Equation [6] is applied for annular flow and for the slug bubble region in slug flow. Dryout occurs when the liquid film cannot wet the total wall perimeter. $\Psi_{\mathrm{e},q}$ is further increased downstream from that point to remove the remaining liquid from the wall. To account for the prevailing phenomena, the maximum of hydrodynamic and heat flux induced entrainment rate is selected.

Equation [6] has been obtained with the assumption of inhibited deposition of droplets. To suppress deposition through the vapor mass flux away from the interface, the following modification to the basic form of [4], $\Psi_\mathrm{d} = 4/Dk\mathrm{C}$, has been developed, based on the experimental data discussed later.

$$\Psi_{\mathrm{d}} = \frac{4}{D}(k - k_q)\frac{\gamma\rho_{\mathrm{l}}}{(\alpha+\gamma)}$$

with

$$k_q = \frac{\rho_{\mathrm{g}}}{0.065\rho_{\mathrm{l}}} V_{\mathrm{g}}$$

and

$$V_{\mathrm{g}} = \Psi_{\mathrm{g,l}}\frac{A}{\rho_{\mathrm{g}} S_{\mathrm{if}}} \qquad [7]$$

In the above equations, S_{if} is the perimeter of the liquid film interface, k is the deposition mass transfer coefficient from [4] and k_q a corresponding suppression coefficient. V_{g} is the vapor velocity perpendicular to the liquid film; for zero evaporation the above correlation is identical with [4]. Further, the deposition rate is limited to positive values. For high heat fluxes, zero deposition rates are obtained which is consistent with the assumption of Milashenko *et al.* (1989), who correlated $\Psi_{\mathrm{e},q}$ as the net entrainment rate. The above correlation is applied for annular flow and for the slug–bubble region in slug flow. The suppression of droplet deposition by the vapor generation has also been modelled by Sugawara and Miyamoto (1990a).

While hydrodynamic entrainment and deposition rates could be tuned to give satisfactory agreement with experiments with constant axial heat flux, this was not possible with varying axial heat flux and the models [6] and [7] had to be included. The set of [4] to [7] account for hydrodynamic entrainment and deposition, heat flux induced entrainment, and deposition inhibition through film evaporation. Thus several physical phenomena are covered and it is therefore recommended.

2.2. *Interfacial momentum transfer*

Another factor which influences the prediction of the dryout location, although much less than entrainment and deposition for the comparisons shown below, is the interfacial momentum transfer. The most common correlation for wavy annular flow is that of Wallis (1969), which relates the friction to the dimensionless film thickness. For thin films the interfacial friction coefficient λ_{i} is approximated by:

$$\lambda_{\mathrm{i}} = 0.02[1 + 75(1-\alpha)] \qquad [8]$$

In addition, entrainment and deposition rates contribute to interfacial momentum transfer. However, sensitivity calculations showed little effect of entrainment and deposition momentum transfer on the dryout quality for the data used here.

2.3. *Post dryout heat transfer coefficient*

The post dryout (PDO) wall temperature is determined by the single-phase, possibly droplet-enhanced steam heat transfer coefficient at the wall and by the steam temperature. The steam temperature itself is also influenced by the evaporation of the liquid droplets. The applied single-phase heat transfer coefficient is given by an ad-hoc correlation for the Nusselt number ($Nu = hD/k$)

$$Nu_{\mathrm{g}} = 0.023 Re_{\mathrm{g,film}}^{0.8} Pr_{\mathrm{g,film}}^{1/3}$$

with

$$T_{\mathrm{film}} = 0.2T_w + 0.8T_{\mathrm{g}} \qquad [9]$$

where the Reynolds and Prandtl numbers ($Re = \rho UD/\mu$, $Pr = \mu\, c_p/k$), $Re_{\mathrm{g,film}}$ and $Pr_{\mathrm{g,film}}$, are evaluated at film temperature T_{film}. Equation [9] is similar to the Colburn (1933) correlation which is, however, based on the bulk temperature in its original form. Other relations have been tried, like the Dittus and Boelter (1930) and the Kutateladze and Borrishanskii (1966) corre-

lations, which include the effect of wall superheat. They all over-predict the heat transfer and consequently under-predict the wall temperature right downstream the dryout point. In this region the droplet evaporation is negligible and thus the wall temperature is determined by the steam-wall heat transfer coefficient. One of the reasons for the too high heat transfer, especially for high pressures, is the high Prandtl number (~1.8 for 10 MPa) of saturated steam, which rapidly drops back to around 1.0, with increasing steam superheat.

The correlations from Heineman (1960); Bishop *et al.* (1965); Hadaller and Banerjee (1969) were specifically derived for superheated steam. They all base the Reynolds and Prandtl numbers on a film temperature which is the average of the wall and bulk temperatures. Contrary to the bulk based heat transfer correlations, these over-predict the wall temperature right downstream the dryout point and require possibly an additional droplet enhancement term.

As [9] includes the effect of the film temperature, and is consistent with low wall superheat, it has been preferred to the above correlations.

Further downstream from the dryout location droplet evaporation becomes important and droplet interfacial area and heat transfer have a significant influence on the wall temperature.

2.4. *Droplet heat transfer, size, and velocity*

For droplet heat transfer, only the resistance from vapor to droplet surface is significant and, consequently, the liquid droplets are assumed to be at saturation condition. Lee and Ryley (1968) proposed the following correlation, which is based on measurements with suspended droplets in superheated steam:

$$Nu_{\mathrm{d}} = 2 + 0.74 Re_{\mathrm{d}}^{0.5} Pr_{\mathrm{g}}^{0.3}$$

with

$$Re_{\mathrm{d}} = \frac{d_{\mathrm{d}} U_{r\mathrm{d}}}{\mu_{\mathrm{g}}} \qquad [10]$$

where d_{d} is the droplet diameter and U_{rd} is the relative droplet velocity defined below by [13].

In the model presented here the droplet diameter is given by

$$d_{\mathrm{d}} = \frac{2 We_c \sigma}{\rho_g U_{\mathrm{sg}}^2} \left(\frac{\gamma}{4.6 \cdot 10^{-7}} \right)^{\frac{2}{9}}$$

with

$$We_c = 5 \qquad [11]$$

In the above equations, U_{sg} is the superficial gas velocity and We_c a critical Weber number ($We = \rho_{\mathrm{g}} U_{\mathrm{sg}}^2 d_{\mathrm{d}}/\sigma$). Together with the droplet heat transfer coefficient, this gives the same dependency of the post dryout mass transfer on superficial steam velocity and droplet volume fraction as the correlation of Webb *et al.* (1982):

$$\Psi_{\mathrm{g},p\mathrm{d}o} \propto \gamma^{\frac{2}{3}} U_{\mathrm{sg}}^2 \qquad [12]$$

The relative droplet velocity is calculated from a correlation proposed by Ishii (1977):

$$U_{\mathrm{rd}} = U_{\mathrm{d}} - U_{\mathrm{g}} = 3 \frac{\sigma}{\rho_g U_{sg}^2} \left(\frac{(g \Delta \rho)^2}{\mu_g \rho_g} \right)^{\frac{1}{3}} \qquad [13]$$

where g is the gravitational constant. The above correlation is applied both for the hydrodynamics and for calculation of the heat transfer coefficients. However, the hydrodynamic effect of the relative droplet velocity is rather small for the data considered for model validation here.

2.5. *Boundary conditions*

Whalley *et al*. (1974) started the calculations at a quality of 1% and with an entrained liquid mass fraction of 99%. These initial conditions are not thought to be realistic, but were found to give reasonable predictions. Only a small effect of the entrance conditions was observed.

Govan (1990) applied modified entrainment and deposition correlations and found the prediction of dryout to be more sensitive to initial conditions. He suggests starting the calculations for annular flow with the assumption of homogeneous flow, an initial void fraction of 50% and equilibrium entrainment, i.e. $\Psi_e = \Psi_d$.

Sugawara (1990b) developed another set of entrainment and deposition correlations and started the simulations with the FIDAS code at the test section inlet with the assumption of homogeneous flow and a parametrically adjusted entrained liquid volume fraction. For his comparison with AERE experiments he found the value of 0.1% for the droplet volume fraction giving the best agreement with the measurements.

The present model confirms the sensitivity reported by Govan. In contrast to the former models, we start the calculations at the test section inlet with well defined boundary conditions, i.e. subcooled liquid flow. After a short distance with bubbly and slug flow, annular flow is selected, according to a generalized minimum slip or maximum void criterion in MONA (Hoyer 1994). As the boiling length usually is too short to achieve an equilibrium entrained fraction, the initial value for the entrained fraction is instead obtained from the upstream history: entrainment and deposition rates are already calculated in the slug–bubble part of the slug flow regime, but the droplets are transported with the liquid film flow and thus have no influence for that flow regime. At the transition to annular flow this droplet fraction is used as the initial value. Consequently, the initial droplet fraction varies, depending on the actual flow parameters. For the validation data base used in this study, the droplet volume fraction is below 7.5% (corresponding to a entrained liquid flow fraction of about 30%) for high pressure cases and well below that for all other cases. The flow regime transitions from slug to annular flow occur well upstream the measured dryout location at void fractions ranging from 65% (10 MPa) to 95% (1 MPa). Sensitivity calculations showed no influence of the exact flow regime transition on the dryout location, unless the transition was well upstream of that point.

2.6. *Solution method*

The three-flow-field model presented here has been implemented in the framework of the MONA code (Hoyer 1994). MONA has been designed as a general simulator for single component two-phase flow systems. It contains a set of seven conservation equations, based on the modelling of three flow fields.

Assuming that the droplet field is moving at approximately the gas velocity, the momentum conservation equations for the gas phase and the droplets are added, yielding a combined momentum equation where the gas–droplet drag term cancels out. The droplet velocity, U_d is specified by an algebraic relation, relative to the gas velocity. Thus only two momentum equations are solved, one for the combined gas/droplet field and one for the continuous liquid field. For energy conservation, mass exchange between the liquid film and the droplet fields is assumed to be prevailing and the two fields consequently will have approximately the same temperature. The energy conservation equations for the liquid film and the droplets can be added and only two energy equations remain, one for gas and one for the combined liquid film and droplets.

In addition to thermodynamic equations of state for each phase, closure relations comprise liquid and gas wall shear, interphase shear as well as wall and interface heat and mass transfer rates. The equations are solved applying the widely used finite difference method (FDM).

Void fraction, pressure drop and flow regimes are not described by separate correlations. MONA applies a more unified approach which treats flow regimes as an integral part of the two-fluid model. A similar methodology has been used previously in the OLGA model, cf. Bendiksen *et al*. (1989).

Table 1. Validation matrix, three different heat flux levels for each point

Heat flux distribution	Diameter (mm)	Pressure(MPa)	Mass flux (kg/m^{2}s)
Constant	14.9	3,5,7,10	1000
Constant	14.9	7	500,1500
Constant	10	7	500,1000,1500
Middle, bottom, top peak	15	7	500,1000,1500
Middle, bottom, top peak	15	1,3,10	1000

Details of the physical and numerical models, as well as the results from basic validation tests have been described by Hoyer (1994), while an application of the model to density wave oscillations in boiling systems is discussed by Hoyer (1995).

3. EXPERIMENTAL DATA AND NUMERICAL DISCRETIZATION

Static dryout experiments based on vertical round tubes have been carried out at the Royal Institute of Technology (KTH) in Sweden (Becker *et al.* 1983, 1992). The loop consisted of a 7 m long test section, a condenser, feed water and main circulation pumps, flow measuring devices and a preheater. Measurements comprise inlet mass flux, subcooling, outer wall temperature along the tube, and pressure drop over the whole test section. The inner wall temperature has been calculated assuming an adiabatic boundary condition at the outer wall. The experiments cover three different diameters, 10, 15 and 25 mm and six different axial power distributions. Temperature distributions were obtained for pressures between 1 and 20 MPa, mass fluxes between 500 and 3000 kg/m^{2}s and heat fluxes between 100 and 3000 kW/m^2. The experimental uncertainties reported by Becker *et al.* (1992) were $\pm 0.8\%$ for the mass flux, $\pm 1.0\%$ for the axial heat flux and ± 3.2 K for the inner wall temperature.

Among the available data, a number of cases have been selected to investigate the influence of the various parameters, as specified in the validation matrix shown in table 1. For each point in the matrix three different heat flux levels have been simulated.

This gives a total of 80 simulations (for one point in the above matrix only two heat flux levels were available). The test section numbering differs from that of the original experimental reports and is given in table 2. The corresponding power shapes are shown in figure 1.

The comparisons from Whalley (1977) and the validation of the FIDAS code against round tube CHF (Sugawara and Miyamoto, 1990a) are based on experiments with constant axial heat flux. Also the work from Govan (1990) is based on a CHF data bank for uniformly heated channels, with the exception of a few comparisons with the low pressure and mass flux, cold-patch data from Bennet *et al.* (1966). Contrary to that, the major part of the measurements used in this study is obtained with a strongly varying axial heat flux distribution.

As no steady state solution is presently available in MONA, transient calculations have been performed, started from an initial state with a water filled test section and run until steady state conditions were reached. A simulation time of 60 s is sufficient for that purpose. Boundary conditions were pressure at the test section outlet and mass flow and subcooling at the inlet. Dependent on the different geometries, the test section has been discretized using 69 or 70 sections. Each flow section is connected to a pipe wall heat structure, containing four concentric segments. The pipe wall heat structure is isolated at the outside. For the test sections with a non-uniform heat flux distribution (non-uniform wall thickness) an average pipe wall thickness has been used. Axial heat conduction is neglected.

Table 2. Test section

Test section	Runs	Powershape
1	1–334	Constant
2	335–510	Constant
3	511–748	Inlet peak
4	749–942	Middle peak
5	943–1110	Outlet peak

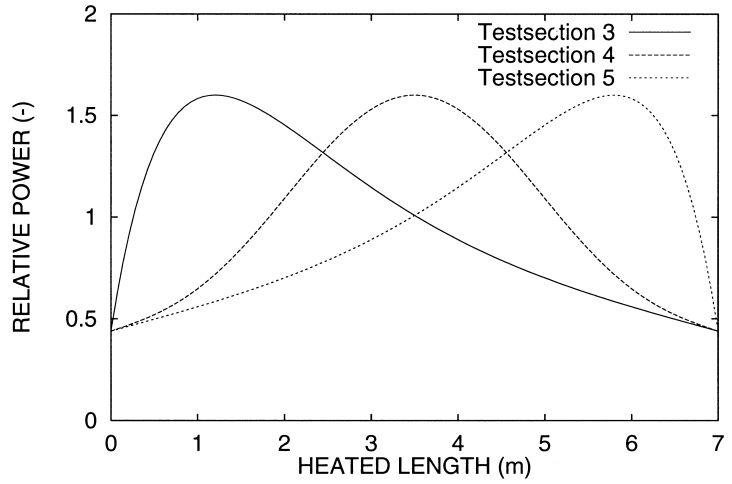

Figure 1. Axial heat flux distributions used in the KTH dryout loop.

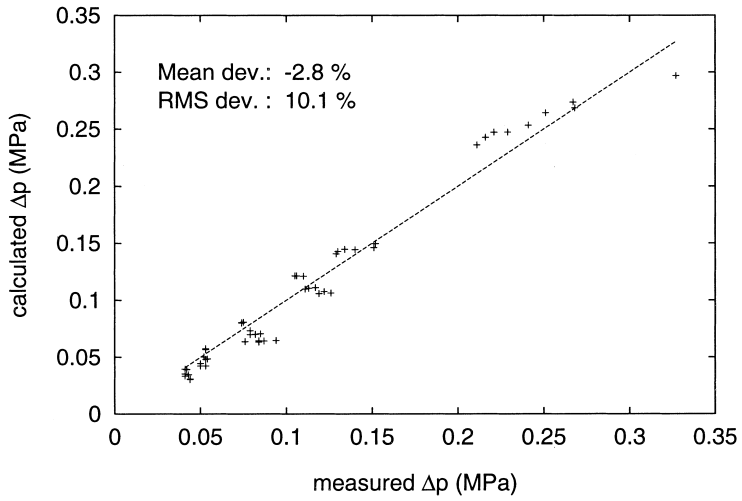

Figure 2. Measured vs calculated pressure drop for test sections 3, 4 and 5.

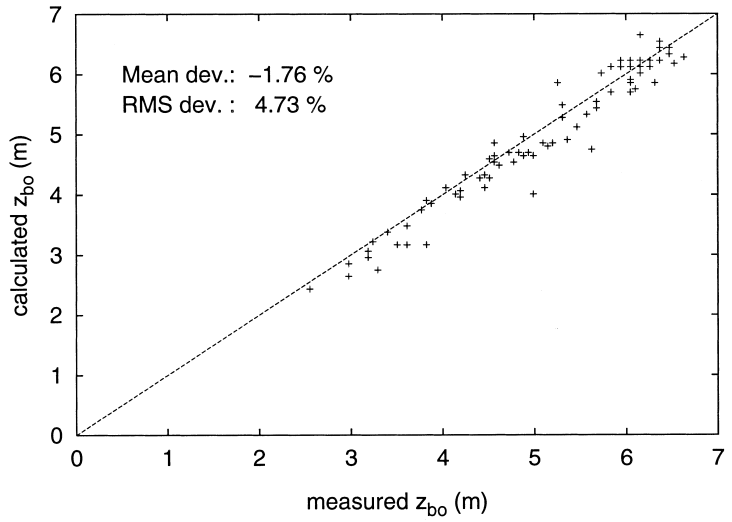

Figure 3. Measured vs calculated dryout location for all test sections.

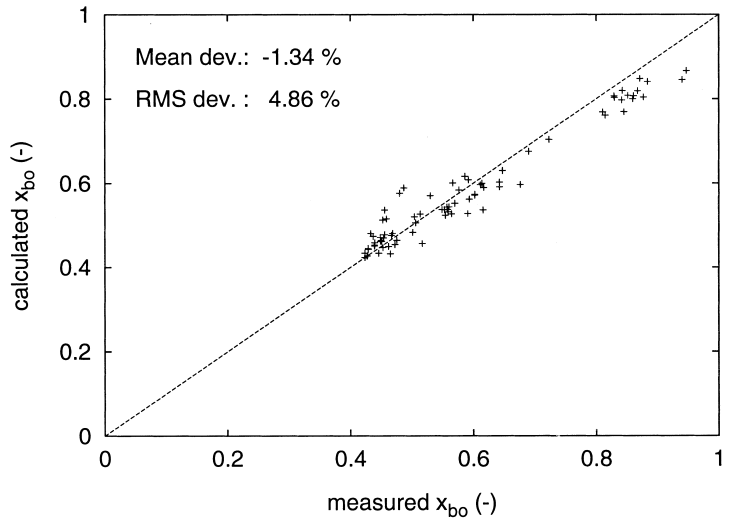

Figure 4. Measured vs calculated dryout quality for all test sections.

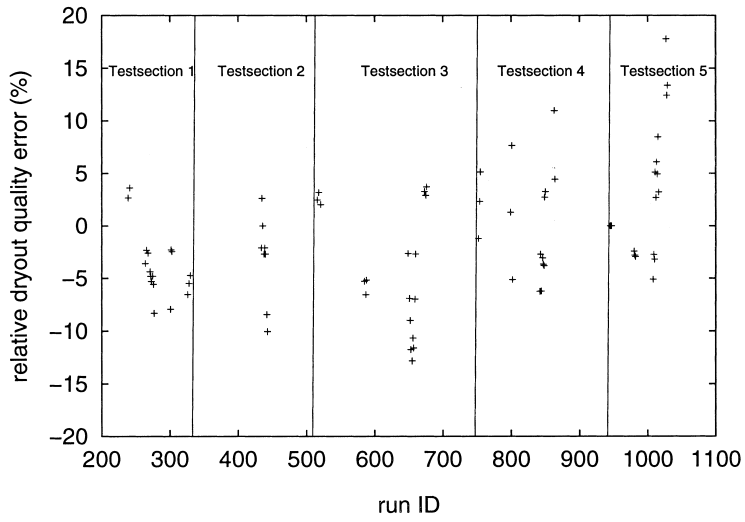

Figure 5. Prediction accuracy for all test sections as a function of test section characteristics: diameter and axial heat flux distribution. Test section characteristics defined in table 2.

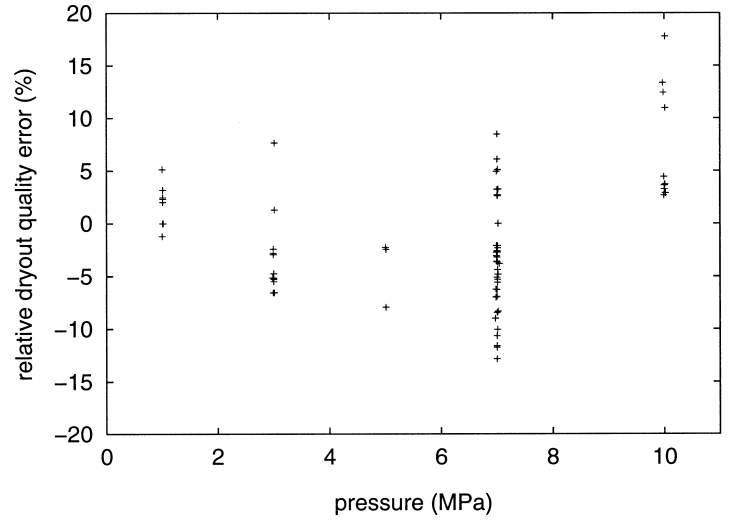

Figure 6. Prediction accuracy as a function of pressure for all test sections.

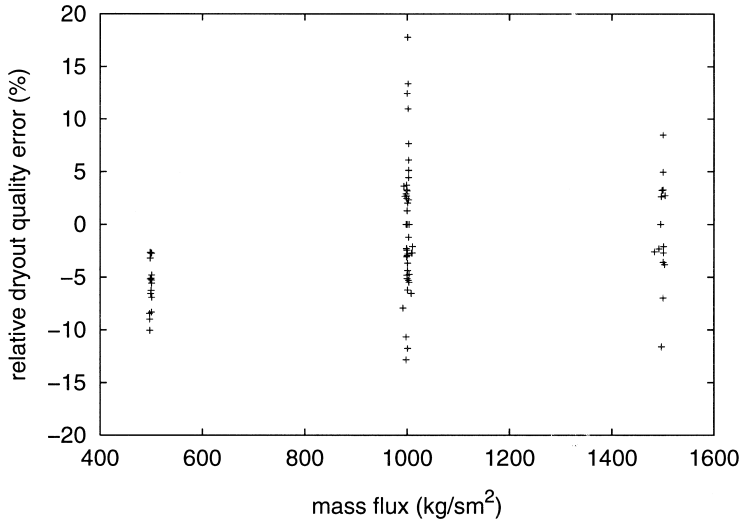

Figure 7. Prediction accuracy as a function of mass flux for all test sections.

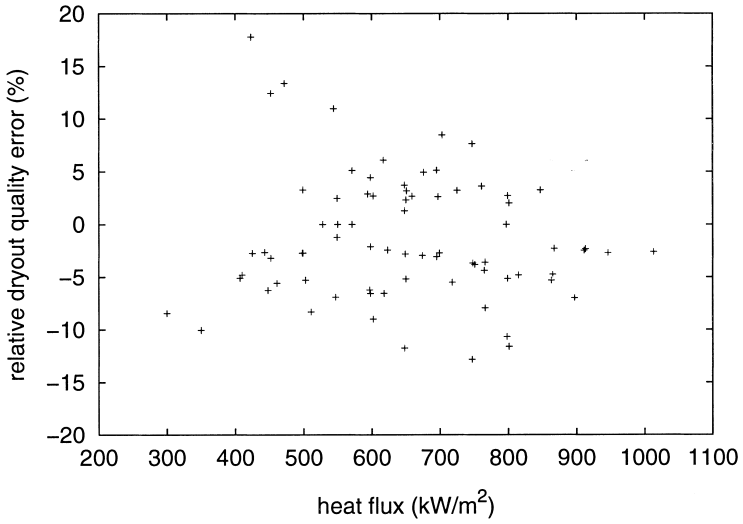

Figure 8. Prediction accuracy as a function of heat flux for all test sections.

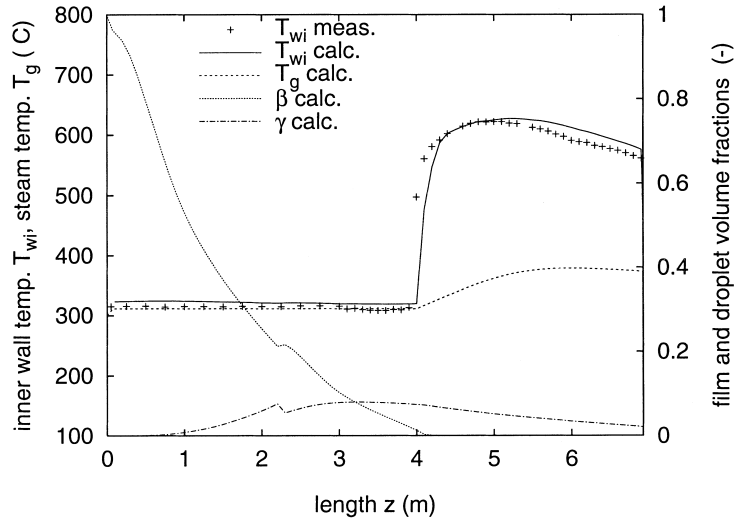

Figure 9. Comparison of inner pipe and vapor temperatures, and film and droplet fractions. Uniform heat flux distribution, $D = 14.9$ mm, $p = 9.99$ MPa, $G = 996$ kg/sm^2, $q_{av} = 659$ kW/m^2.

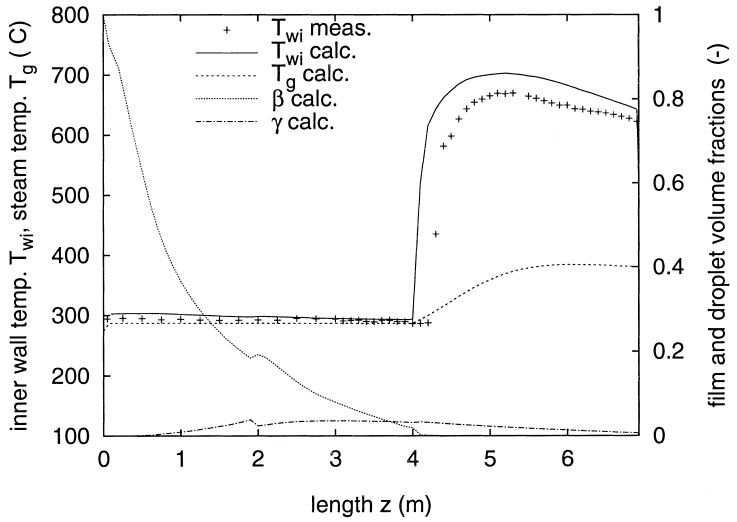

Figure 10. Comparison of inner pipe and vapor temperatures, and film and droplet fractions. Uniform heat flux distribution, $D = 14.9$ mm, $p = 7.01$ MPa, $G = 1002$ kg/sm^2, $q_{av} = 863$ kW/m^2.

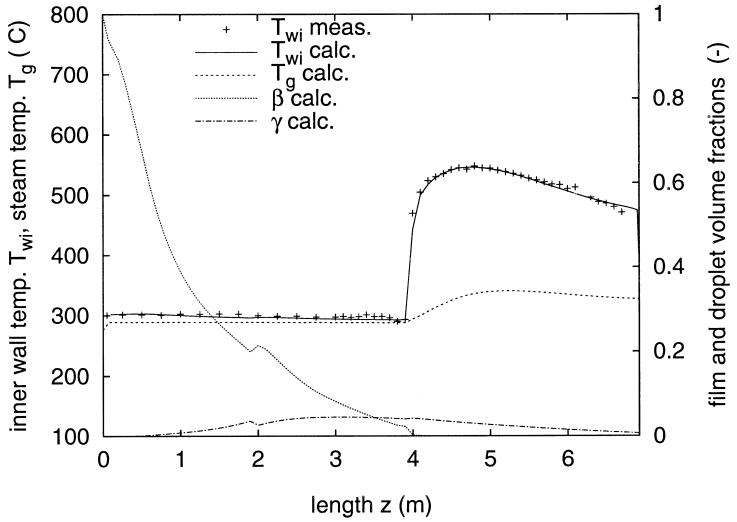

Figure 11. Comparison of inner pipe and vapor temperatures, and film and droplet fractions. Uniform heat flux distribution, $D = 10$ mm, $p = 7.02$ MPa, $G = 1495$ kg/m^2, $q_{av} = 797$ kW/m^2.

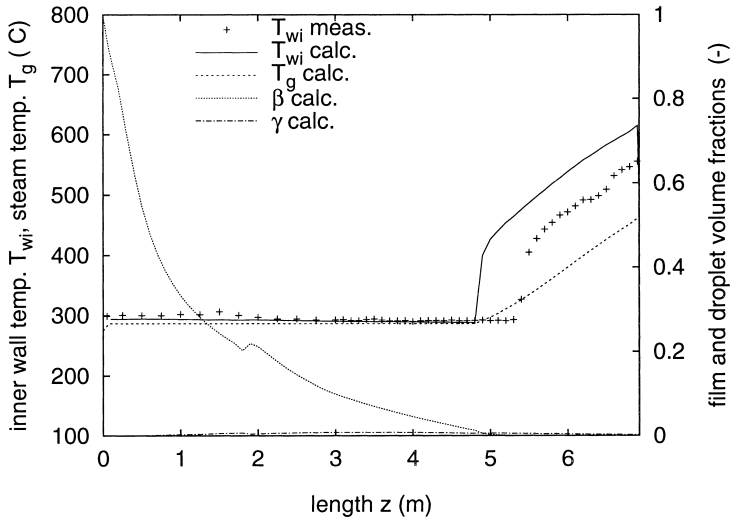

Figure 12. Comparison of inner pipe and vapor temperatures, and film and droplet fractions. Uniform heat flux distribution, $D = 10$ mm, $p = 7.01$ MPa, $G = 497$ kg/sm^2, $q_{av} = 350$ kW/m^2.

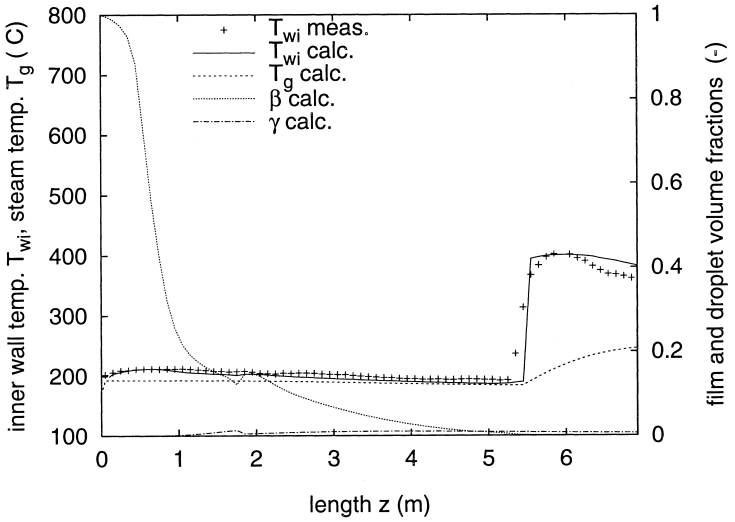

Figure 13. Comparison of inner pipe and vapor temperatures, and film and droplet fractions. Inlet peak heat flux distribution, $D = 15$ mm, $p = 1.01$ MPa, $G = 999$ kg/sm^2, $q_{av} = 549$ kW/m^2.

4. VALIDATION RESULTS

The validation comprises comparison of total pressure drop, dryout location or equilibrium quality and inner pipe temperature. To check the overall performance of the model, the total pressure drop has been compared in figure 2 for the selected runs with test sections 3, 4 and 5. For test section 1, no pressure drop measurements were available and the measurements from test section 2 were discarded due to unrealistic trends. The test section surface roughness was not measured and a value of $\epsilon = 1.0 \times 10^{-5}$ has been assumed. The overall standard and mean deviations between measurements and calculations are also indicated. The predictions show acceptable variation and little systematic deviation.

4.1. *Dryout location*

The calculations have been performed using the phenomenological description of dryout based on the disappearance of the liquid film presented in the section 2. No explicit critical heat flux correlation has been applied and dryout is indicated by the break up of the liquid film and,

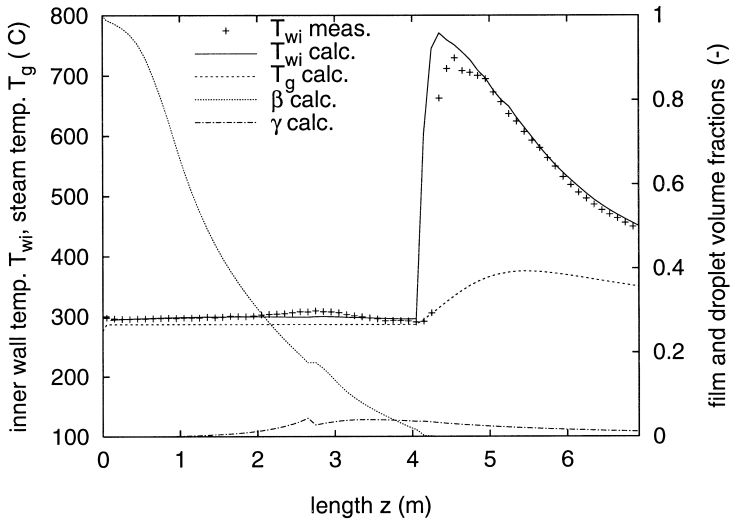

Figure 14. Comparison of inner pipe and vapor temperatures, and film and droplet fractions. Mid peak heat flux distribution, $D = 15$ mm, $p = 7.01$ MPa, $G = 1001$ kg/sm^2, $q_{av} = 748$ kW/m^2.

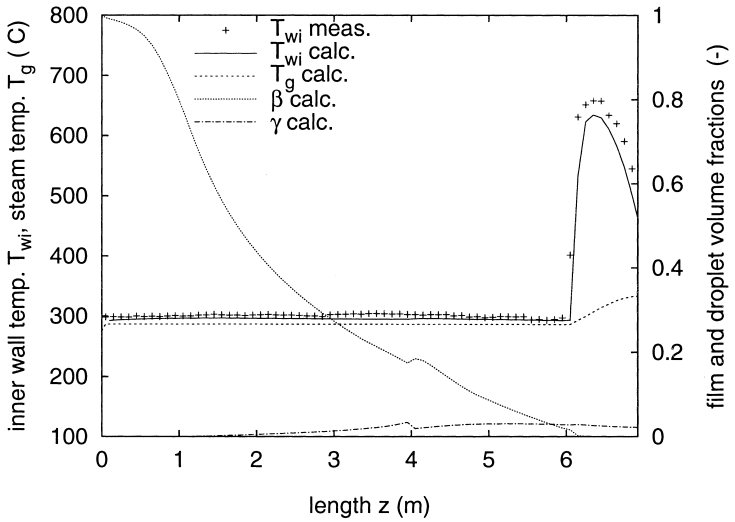

Figure 15. Comparison of inner pipe and vapor temperatures, and film and droplet fractions. Top peak heat flux distribution, $D = 15$ mm, $p = 7.0$ MPa, $G = 1003$ kg/sm^2, $q_{av} = 617$ kW/m^2.

consequently, the change in wall heat transfer coefficient. An overview of the selected validation runs is given in table 1.

Measured and calculated dryout location and equilibrium quality are plotted in figures 3 and 4, respectively. The comparisons demonstrate in general good agreement with a small systematic under-prediction of below 2% and a RMS error of below 5%.

In addition, figures 5–8 show the dependency of the prediction error on important system parameters such as diameter and axial heat flux distribution, pressure, mass- and heat fluxes. While for constant axial heat flux the relative dryout quality error is about 4% for a diameter of 15 mm (test section 1), the average error is less for the 10 mm diameter (test section 2). However, the limited number of selected runs with the 10 mm test section prohibits any firm conclusions. Further, figure 5 indicates a systematic under-prediction of the dryout quality for test section 3 with the bottom-peak heat flux profile. The reason for this behavior is not quite clear, but it may be related to the application of the heat flux induced entrainment correlation [6] for rather thick liquid films.

While the predictions appear to be almost independent of pressure for pressures up to 7 MPa, the dryout quality is somewhat over-estimated for the 10 MPa runs, see figure 6. The heat flux induced entrainment, which is negligible at low pressure, has a considerable contribution at high pressure and the deviation may be related to the influence of [6].

Figure 7 shows a small but systematic under-prediction of dryout quality for low mass fluxes. This is also indicated in figure 4, in the region where the quality is over 80% for the low mass flux runs.

Larger deviations for the low mass flux runs might be expected, as these are not covered by the experimental range upon which the heat flux induced entrainment rate [6] was based. No dependency of the prediction accuracy on the heat flux could be observed in figure 8.

4.2. *Post dryout heat transfer*

Comparison of measured and calculated inner pipe temperatures, vapor temperatures and liquid film and droplet volume fractions for all cases given in table 1 is included here.

Sample plots of these quantities are shown in figures 9–15. For most of the cases with a good match in dryout location, the post dryout wall temperature agrees well, with little systematic deviation and a correct shape of the temperature profile. For the high pressure cases a significant amount of droplets is transported downstream the dryout location. The evaporation of this droplet field causes the vapor velocity to increase and thus also increases the vapor heat transfer at the wall. For the low pressure cases, the entrained fraction is much smaller and the maximum in wall temperature distribution is less pronounced or does not appear at all, cf. Figure 12. Small

deviations in the temperature shape can be found for the 7 MPa, low mass flux and high heat flux cases, where the wall temperature decreases somewhat too fast. A similar deviation in the opposite direction is found for some 1 MPa cases, for test sections with inlet and mid heat flux peak. Post-dryout heat transfer depends on the dryout location and for runs where the dryout quality differs significantly, no conclusions on the post dryout heat transfer can be drawn. However, the overall agreement is very good and compared to other simulations of the KTH data (Abel-Larson *et al.* 1985; Srikantiah 1995), the model presented here shows significant improvement.

5. SUMMARY AND CONCLUSIONS

A method for calculating dryout power and post-dryout heat transfer in tube geometry has been presented. A two-phase, three-field annular flow model is utilized, which uses phenomenological description of dryout based on the disappearance of the liquid film on the wall. Consequently, no explicit critical heat flux correlation has been applied. Entrainment is a key phenomenon in annular flow and entrainment and deposition rates have to be adequately modelled, including the effect of wall heat flux. For the post-dryout heat transfer, the steam–wall and droplet–vapor heat transfers play an important role and determine vapor and surface temperatures.

Static dryout experiments based on vertical round tubes have been carried out at the Royal Institute of Technology (KTH) in Sweden (Becker *et al.* 1983, 1992). From these experiments, 80 runs have been selected for validation, to investigate the influence of the various parameters. The test cases comprise two different tube diameters, 10 and 15 mm, and four different axial power distributions. For the selected runs, the loop pressure varies from 1 to 10 MPa and the mass and heat fluxes from 500 to 1500 kg/m^2s and 300 to 1000 kW/m^2, respectively. Measurements comprise inlet mass flux, subcooling, outer wall temperature along the tube and pressure drop over the whole test section.

The validation covers total pressure drop, dryout location and quality, and inner pipe wall temperature, i.e. forced convective and post-dryout heat transfer. The comparisons of dryout location and quality demonstrate in general good agreement, with a small systematic under-prediction of about 1.5% and a RMS error of below 5%. For the cases with a good match in dryout location, also the post-dryout wall temperatures agree well, with little systematic deviation and correct shapes of the temperature profile.

In addition to the entrainment and deposition correlations of Govan (1990) also the heat flux induced entrainment of Milashenko *et al.* (1989) and modelling of deposition suppression through vapor generation is required to match DO location and PDO heat transfer for the experimental data used here. Without these two models no satisfactory agreement could be obtained for the experiments with a strongly varying axial heat flux. Another important influence comes from the boundary conditions at the onset of annular flow. Best results were achieved with adequate modeling of the upstream flow history based on specific models for bubble and slug flow. Compared to other simulations of the KTH data (Abel-Larson *et al.* 1985; Srikantiah 1995), the present model shows significant improvement.

Acknowledgements—This work has been supported by the Swedish Nuclear Inspectorate (SKI).

REFERENCES

Abel-Larson, H., Olsen, A., Miettinen, J., Siikonen, Rasmussen, J., Sjöberg, A. and Becker, K. (1985) Heat transfer correlations in nuclear reactor safety calculations. NKA (Nordic Liaison Committee for Atomic Energy), *SÅK-5, ISBN 87-550-1109-8*.

Becker, K. M., Ling, C. H., Hedberg, S. and Strand, G. (1983) An experimental investigation of post dryout heat transfer. Department of Nuclear Reactor Engineering, Royal Institute of Technology, *KTH-NEL-33*, Sweden.

Becker, K. M., Askeljung, P., Hedberg, S., Söderquist, B. and Kahlbom, U. (1992) An experimental investigation of the influence of axial heat flux distributions on post dryout heat transfer for flow of water in vertical tubes. Department of Nuclear Reactor Engineering, Royal Institute of Technology, *KTH-NEL-54*, Sweden.

Bendiksen, K. H., Malnes, D., Moe, R. and Nuland, S. (1989) The dynamic two-fluid model OLGA: Theory and application. *J. Petrol. Technol.*, SPE 19451.

Bennet, A. W., Hewitt, G. F., Kearsey, H. A., Keeys, R. K. F. and Pulling, D. J. (1966) Studies of burnout in boiling heat transfer to water in round tubes with non-uniform heating. *AERE-R5076*.

Bishop, A. A., Sandberg, R. O. and Tong, L. S. (1965) Forced convection heat transfer at high pressure after the critical heat flux. *ASME-65-HT-31*.

Bricard, P. and Souyri, A. (1995) Understanding and modelling DNB in forced convective boiling: a critical review. *Proceedings of Two-Phase Flow Modelling and Experimentation*, Rome, Italy.

Celata, G. P., Cumo, M. and Mariani, A. (1994) Assessment of correlations and models for the prediction of CHF in water subcooled flow boiling. *Int. J. Heat Mass Transfer* **37,** 237–255.

Colburn, A. P. (1933) Method of correlating forced convective heat transfer data and a comparison with fluid friction. *Trans. Am. Inst. Chem. Engng* **29,** 174–210.

Dittus, F. W., Boelter, L. M. K. (1930) *Heat transfer in automobile radiators of the tubular type*. Univ. California Publs, Vol. 2, pp. 443-461.

Dallman, J. C., Barclay. G. J. and Hanratty, T. J. (1979) Interpretation of entrainment measurements in annular gas–liquid flows. *Two-Phase Momentum, Heat and Mass Transfer*, ed. F. Durst, G. V. Tsiklauri and N. H. Afgan, McGraw–Hill.

Govan, A. (1990) Modelling of vertical annular and dispersed two-phase flows. PhD Thesis, Imperial College, University of London.

Hadaller, G. and Banerjee, S. (1969) *Heat transfer to superheated steam in round tubes*. Atomic Energy of Canada Limited, Pinawa, Manitoba, Internal Report WDI-147.

Heineman, J. B. (1960) An experimental investigation of heat transfer to superheated steam in round and rectangular channels. Argonne National Laboratories *ANL-6213*.

Hoyer, N. (1994) MONA, A 7-equation transient two-phase flow model for LWR dynamics. *Proceedings of the International Conference on New Trends in Nuclear System Thermohydraulics*, Vol. 1, pp. 271–280.

Hoyer, N. (1995) Validation of the transient two-phase flow model MONA against density wave oscillations. *Proceedings of the International Symposium*. Two-Phase Flow Modelling and Experimentation, Vol. 2, pp. 943–949.

Ishii, M. (1977) One-dimensional drift–flux model and constitutive equations for relative motion between phases in various two-phase flow regimes. *ANL-77-47*.

Katto, Y. (1994) Critical heat flux. *Int. J. Multiphase Flow* **20,** 53–90.

Kutateladze, S. S. and Borishanskii, V. M. (1966) *A Concise Encyclopedia of Heat Transfer*. Pergamon, Oxford.

Lee, K. and Ryley, D. J. (1968) The evaporation of water droplets in superheated steam. *J. Heat Transfer*, 445–451.

Milashenko, V. I., Nigmatulin, B. I., Petukhov, V. V. and Trubkin, N. I. (1989) Burnout and distribution of liquid in evaporative channels of various lengths. *Int. J. Multiphase Flow* **15,** 393–402.

Sugawara, S. and Miyamoto, Y. (1990a) FIDAS: Detailed subchannel analysis code based on the three-fluid and three-field model. *Nucl. Engng Des.* **120,** 147–161.

Sugawara, S. (1990b) FIDAS: Droplet deposition and entrainment modeling based on the three-fluid model. *Nucl. Engng Des.* **122,** 67–84.

Srikantiah, G. (1995) The role of experiments in the development of sub-channel analysis codes for utility applications. *The 3rd International Seminar on Subchannel Analysis*, Stockholm, SKI report 95:16.

Wallis, G. B. (1969) *One-dimensional Two-phase Flow*. McGraw–Hill, NY.

Webb, S. W., Chen, J. C. and Sundaram, R. K. (1982) Vapor generation rate in non-equilibrium convective film boiling. *7th International Heat Transfer Conference*, Munich, paper no. FB45.

Weisman, J. (1992) The current status of theoretically based approaches to the prediction of the critical heat flux in flow boiling. *Nucl. Technol.* **99,** 1–21.

Whalley P. B., Hutchinson P. and Hewitt, G. F. (1974) The calculation of critical heat flux in forced convection boiling. *5th International Heat Transfer Conference*, Tokyo, Paper B6.11.

Whalley, P. B. (1977) The calculation of dryout in a rod bundle. *Int. J. Multiphase Flow* **3,** 501–515.